NANO LETTERS

2006
Vol. 6, No. 6
1287−1291

Tuning Magnetic Domain Structure in Nanoscale $La_{0.7}Sr_{0.3}MnO_3$ Islands

Yayoi Takamura,[†] Rajesh V. Chopdekar,[†,‡] Andreas Scholl,[§] Andrew Doran,[§] J. Alexander Liddle,[||] Bruce Harteneck,[||] and Yuri Suzuki*[,†]

Department of Materials Science and Engineering, University of California, Berkeley, Berkeley, California 94720, Materials Science Division, Lawrence Berkeley National Laboratory, Berkeley, California 94720, School of Applied Physics, Cornell University, Ithaca, New York, 14853, Advanced Light Source, Lawrence Berkeley National Laboratory, Berkeley, California 94720, and Molecular Foundry, Lawrence Berkeley National Laboratory, Berkeley, California 94720

Received March 18, 2006; Revised Manuscript Received May 5, 2006

ABSTRACT

The realization of spin-based devices requires high density, ordered arrays of magnetic materials with a high degree of spin polarization at surfaces. We have synthesized, for the first time, highly spin polarized complex magnetic oxide nanostructures embedded in a paramagnetic matrix by electron beam lithography and ion implantation. Imaging the magnetic domains with X-ray photoemission electron microscopy and magnetic force microscopy reveals a delicate balance between magnetocrystalline, magnetoelastic, and magnetostatic energies that can be tuned by the choice of $SrTiO_3$ substrate orientation, film thickness, island size, and island shape.

Understanding the nature of magnetism at the nanometer length scale is of interest from a fundamental perspective and for the development of next generation spin-based devices. Recent advances in lithography and magnetic domain imaging techniques have facilitated these studies and enabled their application to a wide range of magnetic materials. For structures below a critical dimension, the competition between the magnetostatic energy and exchange energy is predicted to suppress magnetic domain formation, leading to single domain structures. Above this critical dimension, magnetostatic energies often dominate over anisotropy energies to give rise to flux closure domains. However, previous studies have shown that the exact domain pattern depends on parameters such as the particle shape, size, material properties, magnetization history, and film thickness.[1−5] Furthermore, high-density device applications require an understanding of the coupling between magnetic nanostructures.

Thus far the fabrication of magnetic thin film nanostructures has been focused mainly on either the selective etching of a blanket film or templating the growth of the magnetic material in specified locations (e.g., liftoff or electroplating).[1,2] Other studies have produced magnetic nanostructures embedded in a nonmagnetic matrix by precipitation[6] or through spontaneous phase separation during the thin film deposition.[7,8] While these systems may allow for the study of magnetism mediated by a matrix, these nanostructures cannot be synthesized for any arbitrary magnetic material as the processes depend on the details of the phase diagram. Moreover, these approaches lack both long range order and the ability to control the position of the magnetic nanostructures.

While a large body of work exists on the patterning of magnetic metals thin films,[1−5] only a limited number of studies have been performed on complex magnetic oxides.[9−11] For example, the doped rare-earth manganites, $R_{1-x}A_xMnO_3$, where R = trivalent lanthanide and A = divalent alkaline earth, provide a model system for understanding micromagnetism in patterned submicrometer islands and are attractive candidates for memory and sensor applications due to the high degree of spin-polarization and the observation of colossal magnetoresistance (CMR).[12] Furthermore, these properties can be tailored for each application through parameters such as strain,[13,14] oxygen stoichiometry,[15] and chemical substitution.[16,17] Control and understanding of the domain state in CMR materials also provide insight into the premature suppression of spin-polarized tunneling in magnetic tunnel junctions to temperatures well below the Curie temperature of the CMR electrodes.[18,19]

Previously, Wu et al.[9] used optical lithography and ion milling to etch pillars of varying aspect ratio into $La_{0.7}Sr_{0.3}$-

* To whom correspondence may be addressed. E-mail: ysuzuki@berkeley.edu.
[†] Department of Materials Science and Engineering, University of California, Berkeley, and Materials Science Division, Lawrence Berkeley National Laboratory.
[‡] School of Applied Physics, Cornell University.
[§] Advanced Light Source, Lawrence Berkeley National Laboratory.
[||] Molecular Foundry, Lawrence Berkeley National Laboratory.

10.1021/nl060615f CCC: $33.50
Published on Web 05/18/2006

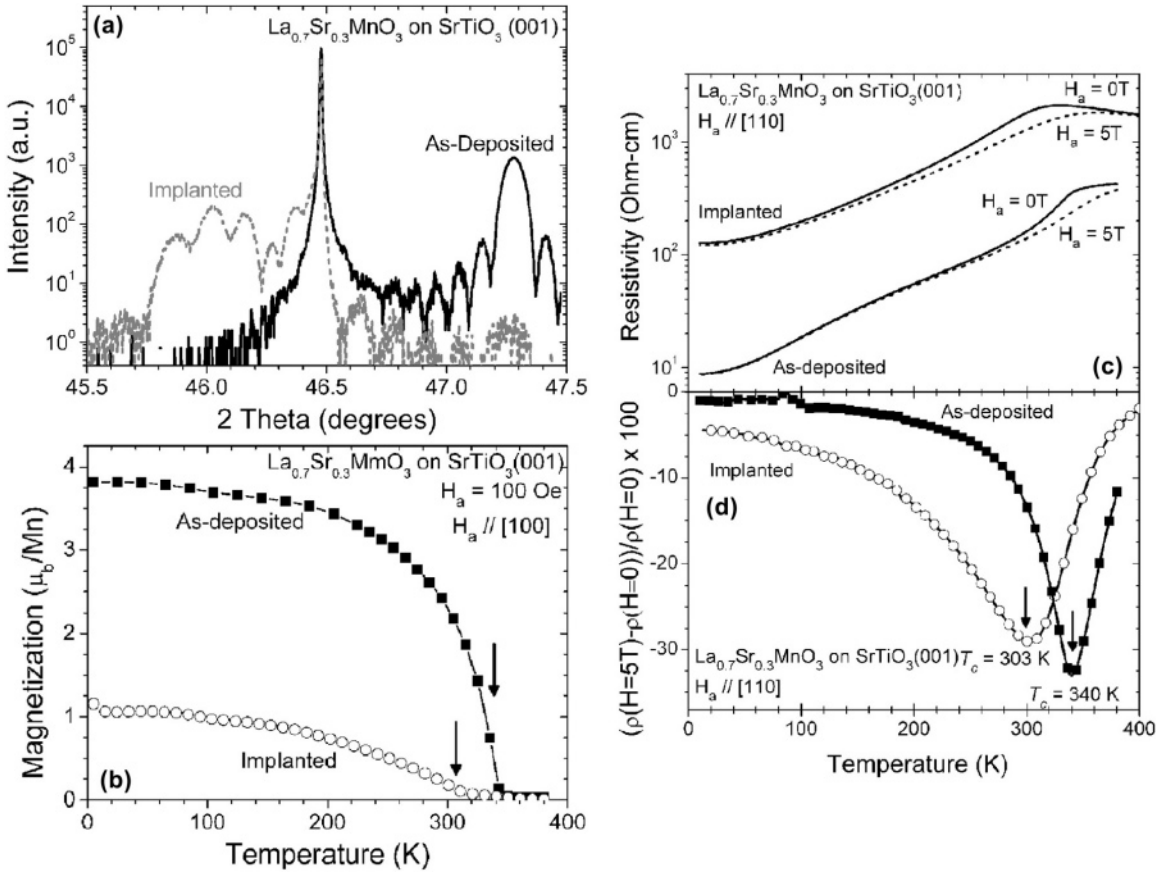

Figure 1. (a) High-resolution XRD $\theta-2\theta$ scans, (b) magnetization, (c) resistivity, and (d) MR as a function of temperature for an unpatterned LSMO film as-deposited and after Ar^+ implantation. The arrows in (b) and (d) indicate the T_c of the films at 340 K for the as-deposited film and at 303 K after Ar^+ implantation.

MnO_3 (LSMO) thin films and used magnetic force microscopy (MFM) to image the domain patterns. The authors found that for circular pillars with diameters ≥ 500 nm, the magnetic properties are dominated by the compressive strain imposed from the $LaAlO_3$ (LAO) substrate with perpendicular snake domains similar to those observed in continuous films. However, the patterning of nanoscale LSMO pillars through electron beam lithography proves to be challenging due to the lack of suitable chemical wet etches and the slow ion milling rate of LSMO.

We have developed a technique to synthesize well-ordered, single crystalline magnetic nanostructures within a paramagnetic matrix using a combination of electron beam lithography followed by ion implantation. This method obviates the need for etching by using ion implantation, not to introduce dopants into the film but instead to cause a local structural distortion that affects the magnetic and transport properties of the film. The matrix ensures a uniform biaxial strain state for the magnetic nanostructures in contrast to partially relaxed magnetic islands that are etched out of a blanket film. Using X-ray photoemission electron microscopy (X-PEEM) and MFM, we have probed the micromagnetism in highly spin polarized LSMO. The magnetic domain structure exists in a delicate balance between shape, magnetocrystalline, magnetostatic, and magnetoelastic energies, which can be tuned by changing the substrate orientation, the film thickness, the island size, and the island shape.

The LSMO films are grown under tensile strain on (001)- and (110)-oriented $SrTiO_3$ (STO) substrates. This choice of substrate orientation allows us to vary the relative contribution of shape, magnetocrystalline, and magnetoelastic energies on the final domain pattern of submicrometer islands. In unpatterned films on (001)-oriented STO substrates, the magnetocrystalline energy dominates over the magnetoelastic energy, resulting in an in-plane 4-fold symmetry with the easy directions along the $\langle 1\bar{1}0\rangle$ directions and the hard directions along the $\langle 001\rangle$ directions.[20] In contrast, for (110)-oriented films, the magnetoelastic energy dominates and the films take on a 2-fold symmetry with the easy direction along the [001] direction and the hard direction along the $[1\bar{1}0]$ direction.[20]

The process flow for creating magnetic islands embedded within a paramagnetic matrix proceeds as follows. First, a thin film ($\sim$60 nm) of LSMO is deposited on a STO substrate by pulsed laser deposition. The KrF laser (248 nm) was operated at 3 Hz and a fluence of $\sim$1.0 J/cm^2, while the substrate temperature was held at 700 °C and the oxygen pressure was 320 mTorr. Second, a double layer mask consisting of 20 nm of poly(methyl methacrylate) (PMMA) and 400 nm of hydrogen silsesquioxane (HSQ) is spin coated and patterned using electron beam lithography. Third, this mask pattern defines regions that are/are not exposed to an Ar^+ ion implantation at 100 keV and a dose of 1×10^{14} cm^{-2}. The mask pattern consists of square, diamond, and

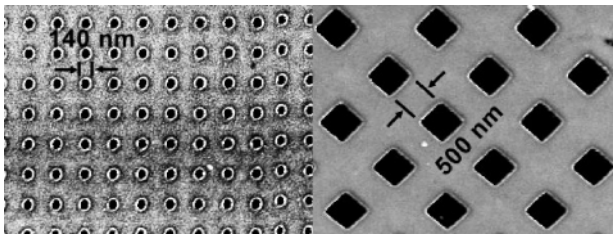

Figure 2. AFM image of 140 and 500 nm diameter magnetic islands in a nonmagnetic matrix after patterning. The matrix regions have expanded by ~10 nm in height due to the Ar^+ implantation relative to the protected islands.

circular islands with diameters ranging from ~140 nm to 1 μm. Stopping and Range of Ions in Matter 2003 simulations[21] predict that the damage profile from this implant condition extends throughout the thickness of the LSMO film while the 400 nm thick HSQ layer is sufficient to stop the Ar^+ ions from penetrating the underlying LSMO film. Fourth, the PMMA layer is used as a lift-off layer to remove the HSQ mask.

The effect of the Ar^+ implantation on the structural, magnetic, and transport properties of an unpatterned LSMO thin film is shown in Figure 1. High-resolution X-ray diffraction (XRD) $\theta-2\theta$ scans around the out-of-plane (002) reflection (Figure 1a) attest to the high quality of the as-deposited LSMO films, displaying thickness fringes on either side of the (002) film peak. The Ar^+ implantation does not amorphize the LSMO film, but instead it modifies the strain state, causing the expansion of the lattice and the displacement of the film peak to the low angle side of the substrate peak. This expansion distorts the crystal structure and effectively changes the Mn−O bond distance and the bond angle, two important parameters in the double exchange mechanism.[22,23] Reciprocal lattice maps (not shown) indicate that the as-deposited film and the implanted film alike are fully strained by the substrate without any mosaic broadening. The magnetization (Figure 1b) of the implanted LSMO film is suppressed significantly at all temperatures in the range of 5−400 K compared to the as-deposited film, with more than an order of magnitude suppression measured at room temperature. Correspondingly, the Ar^+ implantation results in an order of magnitude increase in the resistivity (Figure 1c) of the LSMO film without a large modification to the shape of the resistivity curves as a function of temperature. The magnetoresistance, $MR = (\rho(H = 5\ T) - \rho(H = 0\ T))/\rho(H = 0\ T) \times 100$ (Figure 2d) shows that after the Ar^+ implantation, the metal/insulator transition coincides with the ferromagnetic/paramagnetic transition at a reduced T_c of 303 K compared to 340 K for the as-deposited film and that both transitions occur over a much broader range of temperatures. The observation of CMR behavior and a clear metal/insulator transition in the transport data further support the XRD results indicating that the Ar^+ implantation does not amorphize the LSMO film but leads to a modification of its strain state throughout its entire thickness.

Atomic force microscopy (AFM) images of the final patterned structures are shown in Figure 2 for 140 and 500 nm diameter islands. The expansion of the lattice seen in the XRD data manifests itself as a height difference of ~10 nm for the implanted matrix in relation to the protected islands. This flat surface has several advantages over the traditional pillar structures, including the possibility to deposit subsequent layers on top, the absence of ion milling damage to the sidewalls, and the ease of performing the X-PEEM and MFM domain imaging measurements. The minimum size of the islands is limited by the lateral straggle of the Ar^+ ions during ion implantation, which for a 100 keV implant is approximately 17 nm.[21] This lateral straggle decreases with decreasing implant energy (10 nm for a 50 keV implant), permitting smaller features in thinner films. Furthermore, the magnetic islands exist in a matrix-imposed biaxial strain state in contrast to that of biaxially strained unpatterned films and that of ion-milled pillars, which exist in partially or fully relaxed strain states depending on their aspect ratios.

X-PEEM imaging was carried out on the PEEM2 microscope installed at the Advanced Light Source.[24] Circularly polarized X-rays are incident upon the sample and the emitted secondary electrons from the sample surface are captured by an electron microscope and spatially imaged with a charged couple device camera. Surface sensitivity is limited by the electron escape depth (~5−10 nm) and element specificity is obtained by tuning the photon energy to the absorption edges of the elements. The second column in Figure 3 shows the chemical contrast for 500 nm diameter islands on (001)-oriented STO substrates with varying shape taken at the Mn L_3 absorption edge. Due to changes in the chemical composition and the increase in the resistivity caused by the Ar^+ implantation, the matrix regions have a decreased emission of secondary electrons and appear dark in relation to the protected islands. Domain contrast arises due to X-ray magnetic circular dichroism in which the X-ray absorption depends on the relative orientation of the local magnetization and the polarization vector of the circularly polarized light. Domain images (third column of Figure 3) consist of images taken at the Mn L_3 edge (negative dichroism) divided by images taken at the Mn L_2 edge (positive dichroism). In these images the magnetically easy $\langle 1\bar{1}0 \rangle$ directions point horizontally and vertically while the propagation direction of the X-rays points vertically. In this way, the vertical magnetization components appear as bright/dark regions, while the horizontal magnetization components cannot be distinguished from one another and appear with the same shade of gray. In the demagnetized state, the matrix regions show no domain contrast, while the protected islands show flux closure domains in the square and diamond islands and vortex domains in the circular islands. The lack of sensitivity between left and right magnetization components causes the domain images of the diamond islands to appear as two light/dark domains instead of the flux closure domains shown in the schematic in the first column. The presence of the flux closure domains is confirmed by MFM images as discussed below.

In contrast to X-PEEM, the MFM senses the stray fields emitted from the magnetic domains in the sample. For structures with in-plane magnetization, these stray fields

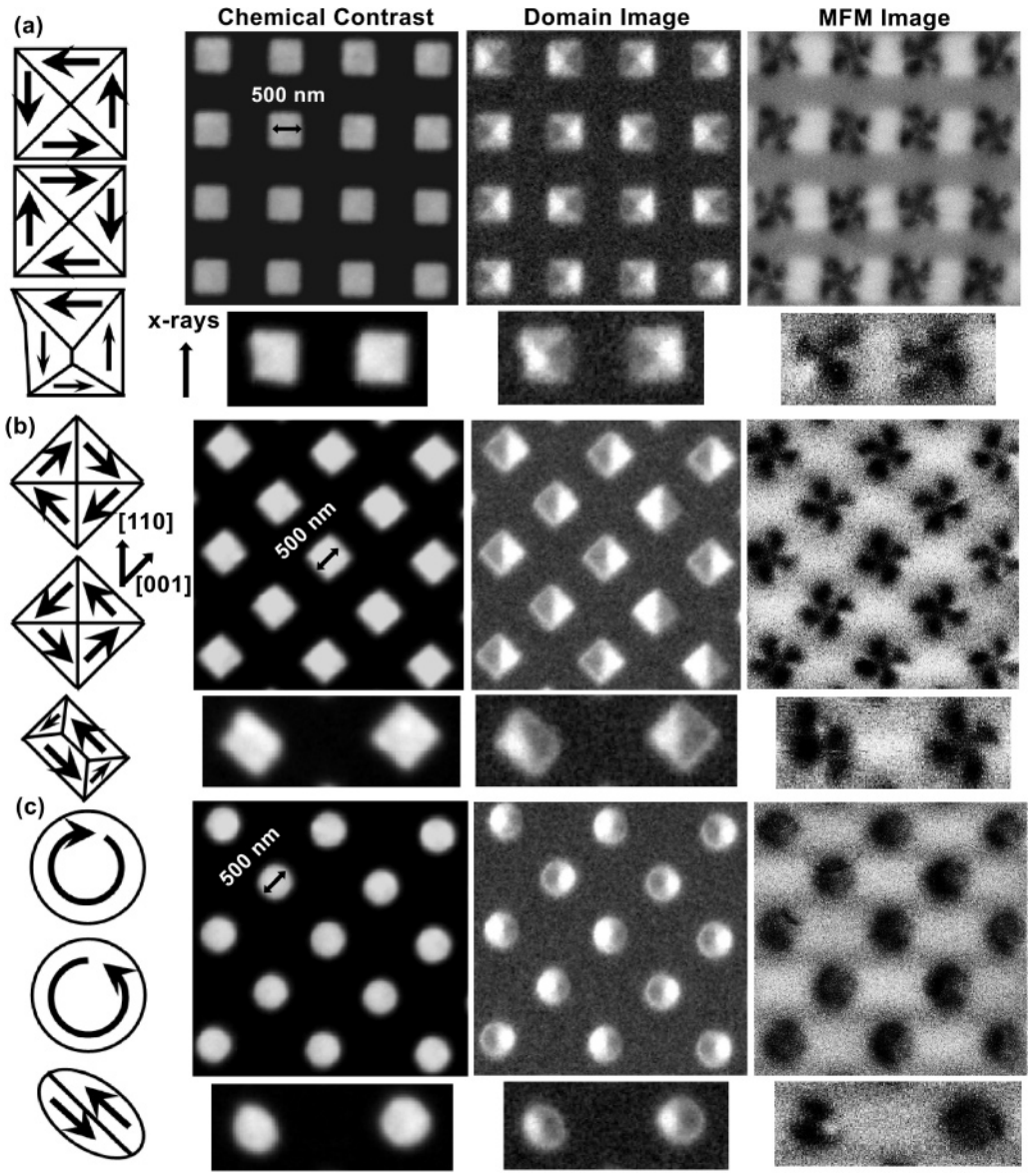

Figure 3. Schematic of the domain pattern, X-PEEM chemical contrast at the Mn L_3 edge, X-PEEM domain contrast, and MFM image of 500 nm diameter islands on (001)-oriented STO substrates with (a) square, (b) diamond, and (c) circular shape. The lower panel to each image shows the effect of distortions of the shape of the island. The LSMO films have been aligned with the magnetically easy ⟨110⟩ directions pointing vertically and horizontally and the propagation direction of the X-rays pointing vertically.

emanate from the domain walls, instead of the domains themselves as in the case of samples with perpendicular magnetization. The fourth column of Figure 3 shows the MFM images for LSMO islands grown on (001)-oriented STO substrates, while Figure 4 shows the case for samples on (110)-oriented STO substrates. For the flux closure domains observed in LSMO islands on (001)-oriented STO substrates, 90° Néel domain walls are located along the diagonals of the squares and diamonds. The resulting images are clockwise or anticlockwise "pinwheels" depending on the chirality of the flux closure domains. These pinwheels are rotated by 45° between the square and the diamond islands, confirming that they both consist of the flux closure domains, with the magnetization direction aligned along the edge of the islands. The vortex domains in the circular islands show almost no contrast in the MFM images, as the moments are contained within the plane of the film without the formation of domain walls. Distortions of the shape of the islands into trapezoids and ellipses lead to modifications of the domain patterns as shown in the lower panels of Figure 3. In all cases, the magnetization prefers to lie along the edge of the islands. In contrast, the islands on (110)-oriented STO substrates show a variation of the domain pattern depending on the shape of the island. In these images, the magnetically easy [001] direction lies horizontally while the hard [1$\bar{1}$0] direction lies vertically. The square islands appear as "distorted pinwheels" with two opposite lobes appearing much larger than the other two lobes. These images suggest that the domain pattern remains a flux closure pattern but that the horizontal domains grow in size relative to the vertical domains. The domains in the diamond and circular islands appear as dark/light lobes pointed in opposite directions, indicating that the domain pattern consists of two horizontal domains aligned along the easy [001] direction.

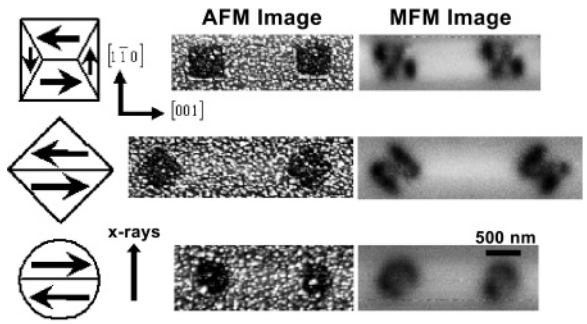

Figure 4. Schematic of the domain pattern, AFM image and MFM image of 500 nm diameter islands on (110)-oriented STO substrates with (a) square, (b) diamond, and (c) circular shape. The LSMO films have been aligned with the magnetically easy [001] direction pointing horizontally.

These domain images demonstrate that for LSMO islands on (001)-oriented STO substrates, the shape of the islands dominates over the crystal field and epitaxial strain effects to determine the domain structure. Calculations based on the magnetostatic energy, the anisotropy energy, and the domain wall energy support these findings and predict that for diameters greater than ~50 nm the flux closure or vortex domain is the energetically favorable configuration for all three shapes studied. These results are in contrast to the work by Wu et al.[15] on LSMO pillars grown on LAO substrates where the perpendicular snake domain patterns were determined by the strain imposed from the substrate and showed little difference compared to continuous films.

The situation on the (110)-oriented STO substrates is more complex due to the uniaxial anisotropy of the LSMO thin film. Using the magnetization data along the hard direction of a 60 nm thick film, we deduce a uniaxial anisotropy constant, $K_u = 1.48 \times 10^5$ ergs/cm^3. This value compares well with the commonly cited value of $K_u = 8.4 \times 10^4$ ergs/cm^3 (ref 14) obtained for a 250 nm thick film. Calculations confirm that the energetically favorable pattern for the diamond and circular islands consists of the two domain pattern, while for the square islands, it is the distorted flux closure domains. The increase in the anisotropy energy on (110)-oriented substrates drives the domain patterns away from the flux closure pattern toward a two-domain pattern. Similar calculations performed varying the thickness of the film between 0 and 100 nm while maintaining a 500 nm island diameter show that the film thickness can be used to tune the domain pattern to consist of either a single domain, a two domain, or a flux closure domain in all three shapes studied. Therefore, our novel patterning technique provides us with the means of controlling the domain patterns in nanoscale magnetic island by the choice of the substrate orientation, the island size, the island shape, and the film thickness.

In conclusion, using a two-step process of electron beam lithography followed by ion implantation, we have patterned LSMO thin films into submicrometer magnetic islands embedded in a paramagnetic matrix. The ion implantation creates a structural distortion which disturbs the magnetic and transport properties in the matrix regions of the LSMO film. A combination of calculations and X-PEEM and MFM images shows that we can control the domain patterns by varying the shape and size of the islands, the film thickness, and the relative magnitudes of the magnetocrystalline and magnetoelastic energies through the choice of the STO substrate orientation. These results provide a platform for performing measurements to determine the influence of domain structure on exchange bias and spin-polarized transport in this class of magnetoresistive materials and for implementing these nanostructures into spin-based devices.

Acknowledgment. The work was funded by the U.S. Department of Energy, Basic Energy Sciences, under Contract No. DE-AC02-05CH11231. The authors thank Dr. Arturas Vailionis at the Stanford Nanofabrication Laboratory for assistance with the XRD analysis.

References

(1) Martin, J. I.; Nogues, J.; Liu, K.; Vicent, J. L.; Schuller, I. K. *J. Magn. Magn. Mater.* **2003**, *256*, 449−501.
(2) Ross, C. A. *Annu. Rev. Mater. Res.* **2001**, *31*, 203−235.
(3) Cowburn, R. P.; Koltsov, D. K.; Adeyeye, A. O.; Welland, M. E.; Tricker, D. M. *Phys. Rev. Lett.* **1999**, *83*, 1042−1045.
(4) Hehn, M.; Ounadjela, K.; Bucher, J.-P.; Rousseaux, F.; Decanini, D.; Bartenlian, B.; Clappert, C. *Science* **1996**, *272*, 1782−1785.
(5) Choe, S.-B.; Acremann, Y.; Scholl, A.; Bauer, A.; Doran, A.; Stohr, J.; Padmore, H. A. *Science* **2004**, *304*, 420−422.
(6) Kraus, G. T.; Lu, Y.-C.; Trancik, J. E.; Mitro, D. M.; Giannelis, E. P.; Thompson, M. O.; Sass, S. L. *J. Appl. Phys.* **1997**, *82*, 1189−1195.
(7) Zheng, H.; Wang, J.; Lofland, S. E.; Ma, Z.; Mohaddes-Ardabili, L.; Zhao, T.; Salamanca-Riba, L.; Shinde, S. R.; Ogale, S. B.; Bai, F.; Viehland, D.; Jia, Y.; Schlom, D. G.; Wuttig, M.; Roytburd, A.; Ramesh, R. *Science* **2004**, *303*, 661−663.
(8) Li, Y. H.; Salamanca-Riba, L.; Zhao, Y.; Ogale, S. B.; Ramesh, R.; Venkatesan, T. *J. Mater. Res.* **2000**, *15*, 1524−1527.
(9) Wu, Y.; Matsushita, Y.; Suzuki, Y. *Phys. Rev. B* **2001**, *64*, 220404.
(10) Ruzmetov, D.; Seo, Y.; Belenky, L. J.; Kim, D.-M.; Ke, X.; Sun, H.; Chandrasekhar, V.; Eom, C.-B.; Rzchowski, M. S.; Pan, X. *Adv. Mater.* **2005**, *17*, 2869−2872.
(11) Li, R.-W.; Kanki, T.; Tohyama, H.-A.; Hirooka, M.; Tanaka, H.; Kawai, T. *Nanotechnology* **2005**, *16*, 28−31.
(12) Ramirez, A. P. *J. Phys.: Condens. Matter* **1997**, *9*, 8171−8199.
(13) Jin, S.; Tiefel, T. H.; McCormack, M.; O'Bryan, H. M.; Chen, L. H.; Ramesh, R.; Schurig, D. *Appl. Phys. Lett.* **1995**, *67*, 557−559.
(14) Suzuki, Y.; Hwang, H. Y.; Cheong, S.-W.; van Dover: R. B. *Appl. Phys. Lett.* **1997**, *71*, 140−142.
(15) Mitchell, J. F.; Argyriou, D. N.; Potter, C. D.; Hinks, D. G.; Jorgensen, J. D.; Bader, S. D. *Phys. Rev. B* **1996**, *54*, 6172−6183.
(16) Hwang, H. Y.; Palstra, T. T. M.; Cheong, S.-W.; Batlogg, B. *Phys. Rev. B* **1995**, *52*, 15046−15049.
(17) Rodriguez-Martinez, L. M.; Attfield, J. P. *Phys. Rev. B* **1996**, *54*, R15622−R15625.
(18) Bowen, M.; Bibes, M.; Barthelemy, A.; Contour, J. P.; Anane, A.; Lemaitre, Y.; Fert, A. *Appl. Phys. Lett.* **2003**, *82*, 233−235.
(19) Viret, M.; Drouet, M.; Nassar, J.; Contour, J. P.; Fermon, C.; Fert, A. *Europhys. Lett.* **1997**, *39*, 545−549.
(20) Berndt, L. M.; Balbarin, V.; Suzuki, Y. *Appl. Phys. Lett.* **2000**, *77*, 2903−2905.
(21) Ziegler, J. F.; Biersack, J. P.; Littmark, U. *The Stopping and Range of Ions in Matter*; Pergamon: New York, 1985.
(22) Patil, S. I.; Shreekala, R.; Lanke, U.; Bhagwat, A.; Ogale, S. B. *Nucl. Instrum. Methods Phys. Res., Sect. B* **1996**, *114*, 42−45.
(23) Chen, C.-H.; Talyansky, V.; Kwon, C.; Rajeswari, M.; Sharma, R. P.; Ramesh, R.; Venkatesan, T.; Melngailis, J.; Zhang, Z.; Chu, W. K. *Appl. Phys. Lett.* **1996**, *69*, 3089−3091.
(24) Anders, S.; Padmore, H. A.; Duarte, R. M.; Renner, T.; Stammler, T.; Scholl, A.; Scheinfein, M. R.; Stohr, J.; Seve, L.; Sinkovic, B. *Rev. Sci. Instrum.* **1999**, *70*, 3973−3981.

NL060615F